Imaging Faults Using Elastic Reverse-Time Migration With Updated Velocities of Waveform Inversion

Ting Chen and Lianjie Huang

Los Alamos National Laboratory, Geophysics Group, Los Alamos NM

Keywords

Elastic reverse-time migration, elastic-waveform inversion, fault, geothermal, multi-component, seismic imaging, velocity model

ABSTRACT

Elastic reverse-time migration (ERTM) has great advantages over other techniques in imaging steep fault zones and complex structures. ERTM imaging requires an accurate velocity model, and elastic-waveform inversion is a promising tool for improving subsurface velocity models. We study how the imaging of fault zones would be improved when combing ERTM with elastic-waveform inversion. We use elastic-waveform inversion to update a velocity model containing several steep fault zones, and employ ETRM to image the faults. We demonstrate using synthetic seismic data for a fault model of the Soda Lake geothermal field that the images of fault zones are greatly improved with the combination of ERTM and elastic-waveform inversion.

1. Introduction

Fault zones may provide paths for hydrothermal flow or confine the boundaries of geothermal reservoirs. Imaging fault zones is therefore crucial for geothermal exploration and enhanced geothermal systems.

Steeply-dipping fault zones and complex subsurface structures have been a great challenge to conventional seismic migration, which uses primary reflections and thus ignores signals from the structures that are illuminated mainly by multiple reflections. Reverse-time migration, on the other hand, solves full-wave equation in heterogeneous media for forward propagation of wavefields from sources and backward propagation of recorded seismic reflection data from receivers. It can handle all complex wave phenomena with no dip limitation, and has been shown as the most promising tool for high-resolution images of complex subsurface structures (Baysal et al., 1983; McMechan, 1983; Whitmore, 1983). Elastic reverse-time migration (ERTM) is needed for multi-component seismic data. ERTM solves the elastic-wave equation and has the potential to reveal structures that are unknown before using conventional seismic migration (Chang and McMechan, 1987; Huang and Albrecht, 2011; Huang et al., 2011).

ERTM requires an accurate velocity model to obtain high-resolution, high-quality images of subsurface structures. In complex geologic environments, one of the most advanced tools for velocity model building is acoustic- and elastic-waveform inversion. Waveform inversion performs forward modeling of seismic wavefield combined with back propagation of residual wavefield to update the velocity model (Virieux and Operto, 2009, and references therein). It has been shown that waveform inversion provides improved velocity models compared to traditional ray-based tomographic approaches (e.g., Vigh et al., 2010).

We have recently developed novel ERTM and elastic-waveform inversion methods to address their challenges for imaging and inversion of complex structures (Zhang et al., 2012; Chen and Huang, 2013). In this work, we combine our ERTM method with our elastic-waveform inversion algorithm to enhance images of steeply-dipping fault zones. We demonstrate the improvement using synthetic seismic data for a model from the Soda Lake geothermal field containing several steep faults.

2. Method

Seismic migration produces subsurface images from seismic reflection data with a velocity model obtained using velocity analysis. Such velocity models are often not accurate for complex structures. An accurate velocity model is particularly important for directly imaging steeply-dipping fault zones. We use elastic-waveform inversion to improve velocity models for both compressional and shear waves, and then perform ERTM with these updated velocities to enhance images of steeply-dipping fault zones.

2.1 Elastic-Waveform Inversion

Elastic-waveform inversion can improve velocity models obtained with velocity analysis, but often reconstructs poorly the deep region of the model because of geometrical spreading and defocusing effects. To reduce these undesirable effects, we use the wave-energy-based precondition approach developed by Zhang et al. (2012) to update velocity models for ERTM. This approach uses forward propagated wavefields from sources and backward propagated synthetic wavefields from receivers to scale the gradients used to update velocity models. It has been shown that this new method converges faster and reconstructs better the faults and the deep regions compared to conventional methods.

2.2 Elastic Reverse-Time Migration

The conventional imaging condition in reverse-time migration can be implemented as

$$I(\mathbf{x}) = \int_0^t s(\mathbf{x},\tau) r(\mathbf{x}, t-\tau) d\tau, \tag{1}$$

where $s(\mathbf{x},\tau)$ is the forward propagation wavefield from a source at location $\mathbf{x}$ and time $\boldsymbol{\tau}$, $r(\mathbf{x}, t-\tau)$ denotes the backward propagation wavefield from receivers, and t represents the maximum record time.

The conventional imaging condition usually generates high-amplitude, low-wavenumber image noise. To eliminate these image artifacts, we separate the forward and backward propagation wavefields into downgoing, upgoing, leftgoing, and rightgoing wavefields, and use these wavefields to form multiple images rather than one image in the conventional ERTM (Denli and Huang, 2008). The downward-looking (I^d), upward-looking (I^u), left-looking (I^l), and right-looking (I^r) images are obtained by the cross correlations of the separated wavefields propagating along the opposite directions:

$$\begin{aligned} I^d(\mathbf{x}) &= \int_0^t s^{+z}(\mathbf{x},\tau) r^{-z}(\mathbf{x}, t-\tau) d\tau, \\ I^u(\mathbf{x}) &= \int_0^t s^{-z}(\mathbf{x},\tau) r^{+z}(\mathbf{x}, t-\tau) d\tau, \\ I^l(\mathbf{x}) &= \int_0^t s^{-x}(\mathbf{x},\tau) r^{+x}(\mathbf{x}, t-\tau) d\tau, \\ I^r(\mathbf{x}) &= \int_0^t s^{+x}(\mathbf{x},\tau) r^{-x}(\mathbf{x}, t-\tau) d\tau, \end{aligned} \tag{2}$$

where "$+z$", "$-z$", "$-x$", and "$+x$" denote downgoing, upgoing, leftgoing, and rightgoing wavefields, respectively. The cross correlations of wavefields from opposite directions along the x- and z-axis give images of vertical (with steep dips) and horizontal (with shallow dips) reflectors, respectively.

During elastic-wave propagation, compressional (P) and shear (S) waves can be converted to one another. Because of the polarization of converted waves, the conventional imaging condition is no longer valid. Destructive interference occurs when stacking PS or SP images with mixed signs of the polarization. Because the signs of converted PS and SP waves depend on the directions of incident waves relative to a reflector, we can obtain coherent images by correcting for the signs in the angle domain.

We employ an extended angle-domain imaging condition to produce PS and SP images (Yan and Sava, 2008):

$$I(\mathbf{x},\lambda) = \int s(\mathbf{x}-\lambda,\tau) r(\mathbf{x}+\lambda, t-\tau) d\tau, \tag{3}$$

where λ is the cross correlation lag in space. The average angle between incidence and reflected waves, θ, can be computed using

$$\tan^2\theta = \frac{(1+\gamma)^2 |\mathbf{k}_\lambda|^2 - (1-\gamma)^2 |\mathbf{k}_\mathbf{x}|^2}{(1+\gamma)^2 |\mathbf{k}_\mathbf{x}|^2 - (1-\gamma)^2 |\mathbf{k}_\lambda|^2} \tag{4}$$

where γ is the ratio between the velocity of an incident wave and that of a reflected wave. The wavenumbers $\mathbf{k}_\lambda$ and $\mathbf{k}_\mathbf{x}$ are defined using the source and receiver wavenumbers $\mathbf{k}_\mathbf{s}$ and $\mathbf{k}_\mathbf{r}$ as $\mathbf{k}_\lambda = \mathbf{k}_\mathrm{r} + \mathbf{k}_\mathrm{s}$ and $\mathbf{k}_\mathrm{x} = \mathbf{k}_\mathrm{r} - \mathbf{k}_\mathrm{s}$, and can be obtained from $I(\mathbf{x}, \lambda)$ in equation (3). The angle-domain image gather $I(\mathbf{x},\theta)$ is then obtained from $I(\mathbf{x}, \lambda)$ using equation (4). The angle-domain migration image is given by

$$A(\mathbf{x}) = \int I(\mathbf{x},\theta)\, d\theta. \tag{5}$$

We use separated wavefields to generate the angle-domain images, and denote the migration images obtained using separated wavefields together with an angle-domain imaging condition as A_{pp}, A_{ps}, A_{sp}, and A_{ss}, and those produced directly

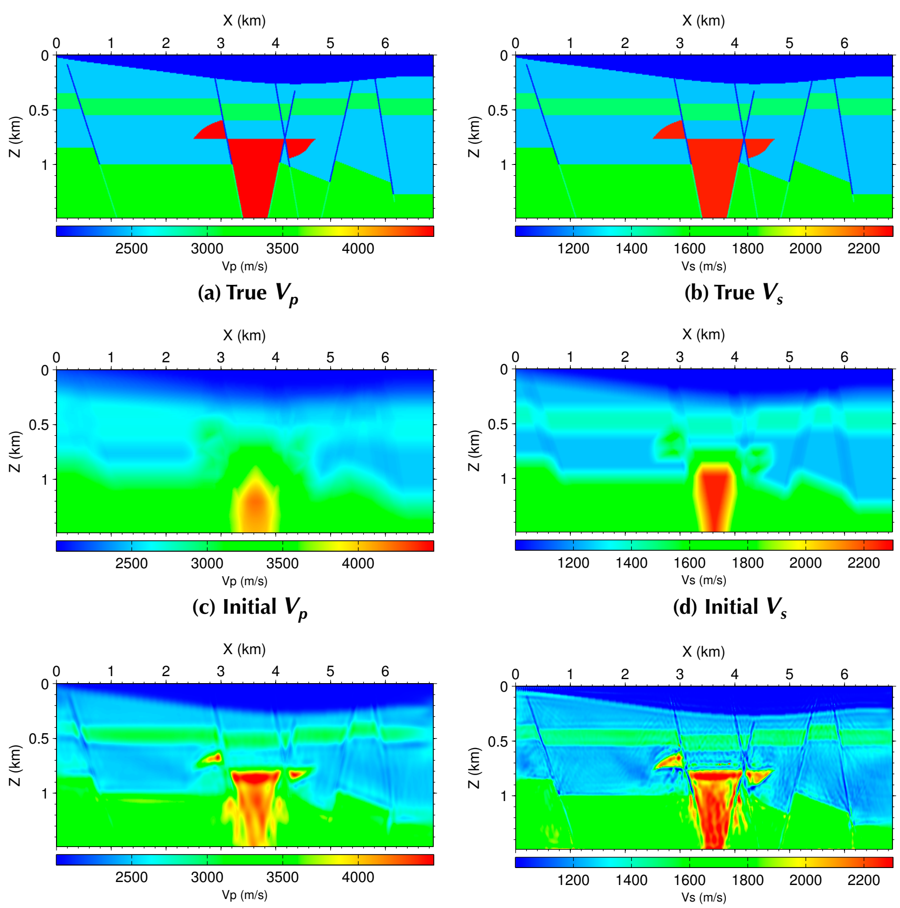

(a) True V_p **(b) True V_s**

(c) Initial V_p **(d) Initial V_s**

(e) Inversion result of V_p **(f) Inversion result of V_s**

Figure 1. Panels in (a) and (b) are P-wave and S-wave velocity models built using geologic features found at the Soda Lake geothermal field. Panels in (c) and (d) are the smoothed initial velocity models for elastic-waveform inversion. The resulting models obtained using elastic-waveform inversion are depicted in (e) and (f).

from separated wavefields as I_{pp}, I_{ps}, I_{sp}, and I_{ss}. Each of these images has downward-looking, upward-looking, left-looking, and right-looking images obtained using separated wavefields propagating along different directions.

3. Imaging Fault Zones for a Soda Lake Velocity Model

We use a velocity model from the Soda Lake geothermal field to validate the improved capability of ERTM for imaging fault zones when combined with elastic-waveform inversion. The model is constructed using the geologic interpretation result of a prestack migration image obtained at the Soda Lake geothermal field. This model consists of five stratigraphic layers and six steeply-dipping fault zones with the width of 25 m (Figs. 1a-b). The model also contains high-contrast basalt units, resulting in a large contrast in P-wave velocity varying from 2000 m/s in the sediment to 4500 m/s in the basalt. Velocity and density values of the fault zones are 15% lower than those of the surrounding layers. The ratio of P-wave and S-wave velocities is two.

For elastic-waveform inversion, we smooth the slowness of the models in Figs. 1a-b over two wavelengths for the central frequency of 10 Hz (Gray, 2000), and use these smoothed models as the starting models (Figs. 1c-d). We generate synthetic multi-component elastic data for the original models in Figs. 1a-b with 172 explosive sources at the top surface using a high-order finite-difference elastic-wave scheme with a perfectly-matched-layer absorbing boundary condition. We perform elastic-waveform inversion using the synthetic data and the smoothed models as the initial models to obtain improved P-wave and S-wave velocity models, as shown in Figs. 1e-f. Both the horizontal layers and fault zones in Figs. 1e-f are much more manifested than the starting models.

We study how the improvement in the velocity models obtained with elastic-waveform inversion contributes to ERTM images, particularly for imaging steeply-dipping fault zones. First, we generate synthetic multi-component elastic reflection data using the true models in Figs. 1a-b. Then, we conduct ERTM with the initial models (Figs. 1c-d) and compare the images with those obtained using the updated models from elastic-waveform inversion (Figs. 1e-f). A total of 85 explosive sources are used. The wavefield-separation imaging condition is used to obtain both PP and PS images. The angle-domain imaging condition is further employed to obtain the converted PS images.

Figure 2 shows the PP images generated using the smoothed initial models, and Fig. 3 depicts the PP images produced using the elastic-waveform inversion models. Comparing with the PP images yielded using the smoothed initial models (Figs. 2c-d), the PP images obtained using the elastic-waveform inversion models (Figs. 3c-d) show fault zones more clearly. The fault zones in Figs. 3c and 3d are not only more straight (e.g., the regions within the red ellipses in the figures), but also more continuous (e.g., the regions within the blue ellipses in the figures). No significant difference is found for the images of horizontal layers using the smoothed initial models (Fig. 2b) and the elastic-waveform inversion models (Fig. 3b). The background low-wavenumber noise in the PP image

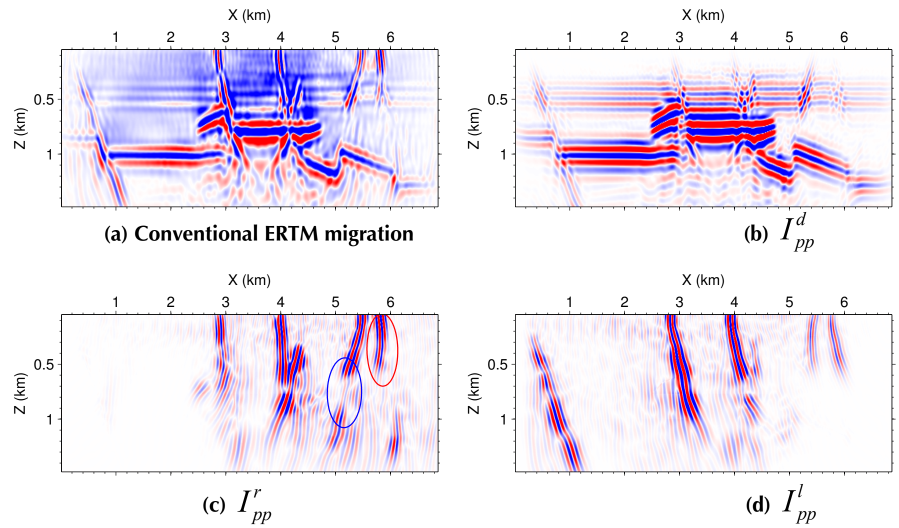

Figure 2. PP images obtained using the smoothed velocity models in Figs. 1c-d: (a) The conventional ERTM image, (b) downward-looking image I_{pp}^{d}, (c) right-looking image I_{pp}^{r}, and (d) left-looking image I_{pp}^{l}. Colored ellipses are for comparison with Fig. 3.

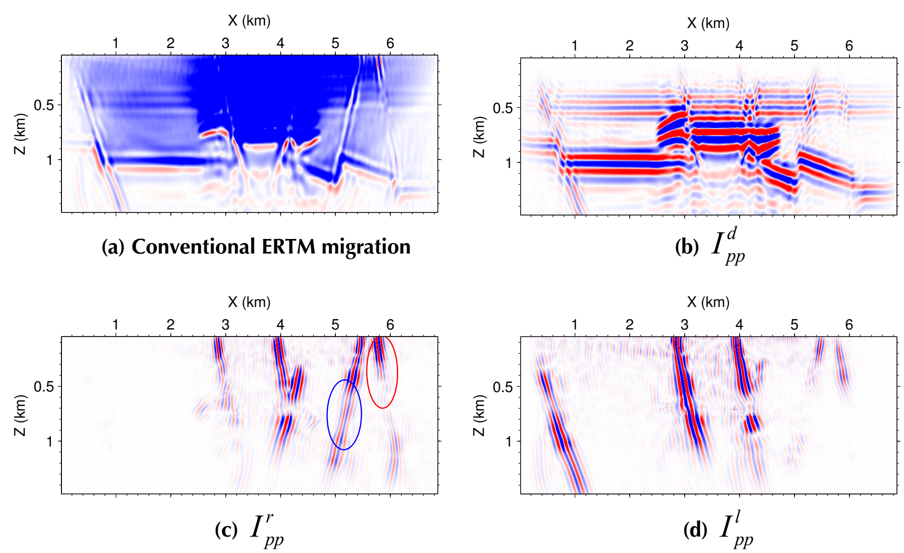

Figure 3. PP images produced using the improved velocity models in Figs. 1e-f: (a) The conventional ERTM image, (b) downward-looking image I_{pp}^{d}, (c) right-looking image I_{pp}^{r}, and (d) left-looking image I_{pp}^{l}. Colored ellipses are for comparison with Fig. 2.

produced using the smoothed initial models (Fig. 2a) is weaker than that in the PP image generated using the elastic-waveform inversion models (Fig. 3a). This is because reflection wavefields in ERTM with the smoothed models are much weaker and do not well coincide with the back propagated wavefields compared to those in ERTM with the elastic-waveform inversion models.

For the PS images, angle-domain analysis is used to correct for the polarization, and results in much more coherent images for both the fault zones and horizontal layers (Figs. 4c, 4e, 4g, in comparison with Figs. 4b, 4d, 4f). Similar to the case of PP images, the fault zones are better imaged using the updated velocity models from elastic-waveform inversion than with the smoothed initial models (e.g., comparing the regions within the ellipses in Figs. 4e and 5e). PS images have higher resolution compared with PP images because of the shorter wavelength of S waves than that of P waves.

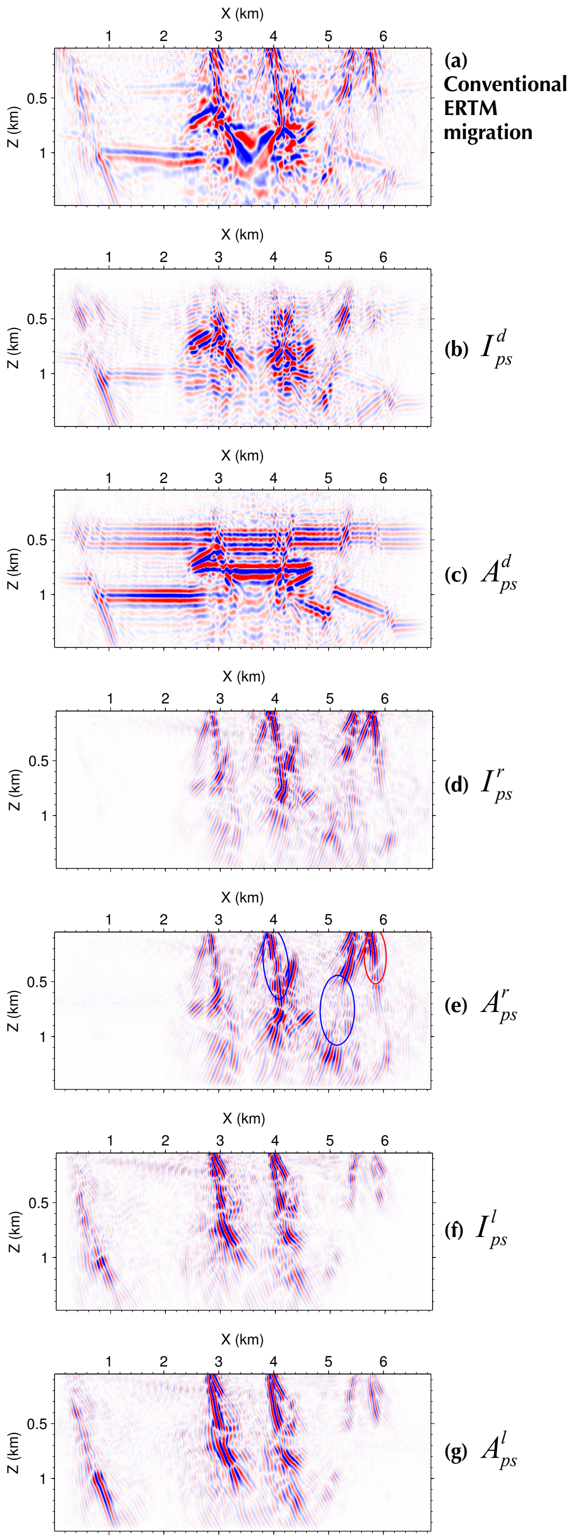

Figure 4. PS images produced using the smoothed velocity models in Figs. 1c-d: (a) The conventional ERTM image, (b) downward-looking image I^d_{ps}, (c) downward-looking angle-domain image A^d_{ps}, (d) right-looking image I^r_{ps}, (e) right-looking angle-domain image A^r_{ps}, (f) left-looking image I^l_{ps}, and (g) left-looking angle-domain image A^l_{ps}. Colored ellipses are for comparison with Fig. 5.

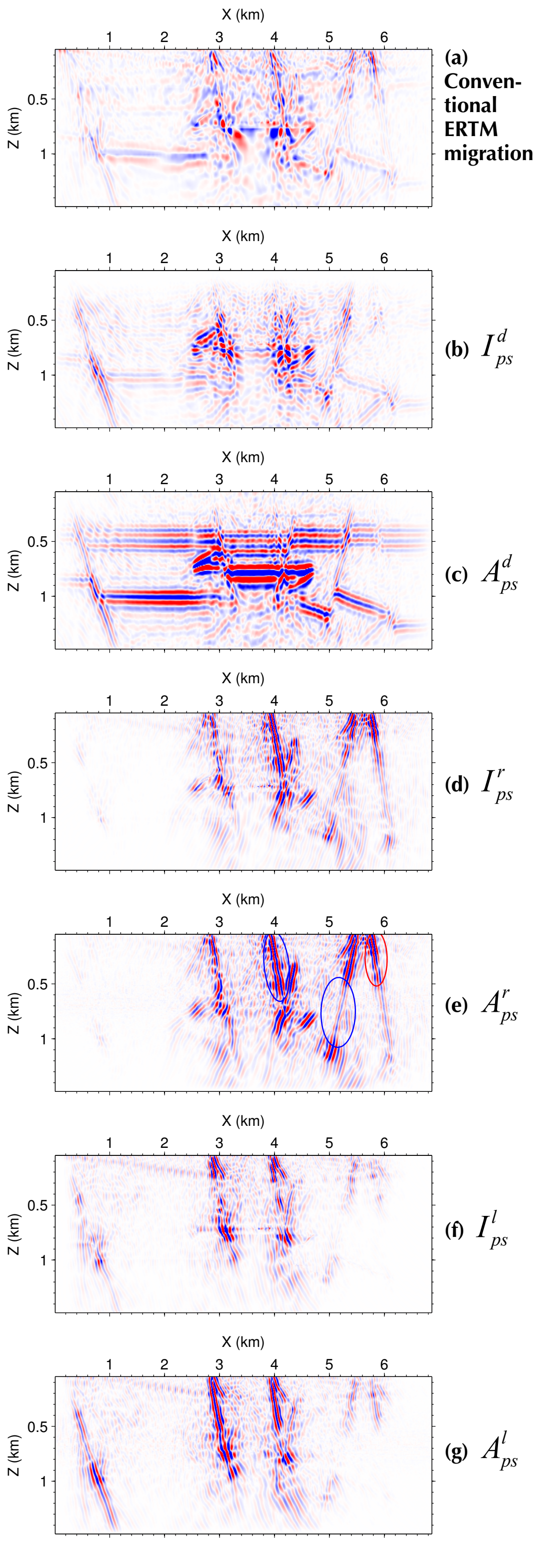

Figure 5. PS images generated using the improved velocity models from elastic-waveform inversion in Figs. 1e-f: (a) The conventional ERTM image, (b) downward-looking image I^d_{ps}, (c) downward-looking angle-domain image A^d_{ps}, (d) right-looking image I^r_{ps}, (e) right-looking angle-domain image A^r_{ps}, (f) left-looking image I^l_{ps}, and (g) left-looking angle-domain image A^l_{ps}. Colored ellipses are for comparison with Fig. 4.

4. Conclusions

We have explored the use of updated velocity models obtained with elastic-waveform inversion for improving elastic reverse-time migration, particularly for imaging steeply-dipping fault zones. We have demonstrated using synthetic seismic data for a Soda Lake geothermal model that elastic-waveform inversion significantly improves both compressional- and shear-wave velocity models, and elastic reverse-time migration using the updated velocity models results in more straight and continuous images of steep fault zones compared to those produced with the initial models. Using an accurate velocity model is particularly important for directly imaging steeply-dipping fault zones.

Acknowledgements

This work was supported by the Geothermal Technologies Office of the U.S. Department of Energy through contract DE-AC52-06NA25396 to Los Alamos National Laboratory. The computation was performed on super-computers provided by the Institutional Computing Program of Los Alamos National Laboratory. We thank Magma Energy (U.S.) Corp. for providing us with migration images and James Echols for his help in building the velocity models for the Soda Lake geothermal field.

References

Baysal, E., D. Kosloff, and J. Sherwood, 1983. "Reverse time migration," Geophysics, 48, 1514–1524.

Chang, W. F., and G. A. McMechan, 1987. "Elastic reverse-time migration," Geophysics, 52, 1365–1375.

Chen, T., and L. Huang, 2013. "Directly imaging steep fault zones using multicomponent seismic data," Proceedings of the Thirty-Eighth Workshop on Geothermal Reservoir Engineering, Stanford University.

Denli, H., and L. Huang, 2008. "Elastic-wave reverse-time migration with a wavefield-separation imaging condition," 78th Annual International Meeting, SEG, Expanded Abstracts, 2346–2350.

Gray, S. H., 2000. "Velocity smoothing for depth migration: How much is too much?," 70th Annual International Meeting, SEG, Expanded Abstracts, 1055–1058.

Huang, L., and M. Albrecht, 2011. "Seismic and magneto-telluric imaging for geothermal exploration at Jemez pueblo in New Mexico," Proceedings of the Thirty-Sixth Workshop on Geothermal Reservoir Engineering, Stanford University, 944–949.

Huang, L., S. Kelley, Z. Zhang, K. Rehfeldt, M. Albrecht, and G. Kaufman, 2011. "Imaging faults with reverse-time migration for geothermal exploration at Jemez Pueblo in New Mexico," Geothermal Resources Council Transactions, 35, 833–837.

McMechan, G. A., 1983. "Migration by extrapolation of time-dependent boundary values," Geophysical Prospecting, 31, 413–420.

Vigh, D., B. Starr, J. Kapoor, and H. Li, 2010. "3D full waveform inversion on a Gulf of Mexico WAZ data set," 80th Annual International Meeting, SEG, Expanded Abstracts, 957–961.

Virieux, J., and S. Operto, 2009. "An overview of full-waveform inversion in exploration geophysics," Geophysics, 74, WCC1–WCC26.

Whitmore, N., 1983. "Iterative depth migration by backward time propagation," 53rd Annual International Meeting, SEG, Expanded Abstracts.

Yan, J., and P. Sava, 2008. "Isotropic angle-domain elastic reverse-time migration," Geophysics, 73, 229–239.

Zhang, Z., L. Huang, and Y. Lin, 2012. "A wave-energy-based precondition approach to fullwaveform inversion in the time domain," 82nd Annual International Meeting, SEG, Expanded Abstracts.